

Multiplexed Optical Operation of Distributed Nanoelectromechanical Systems Arrays

A. Sampathkumar and K. L. Ekinci*

Mechanical Engineering Department and the Photonics Center, Boston University, Boston, Massachusetts 02215, United States

T. W. Murray*

Department of Mechanical Engineering, University of Colorado at Boulder, Boulder, Colorado 80309, United States

ABSTRACT: We report a versatile all optical technique to excite and read-out a distributed nanoelectromechanical systems (NEMS) array. The NEMS array is driven by a distributed, intensity modulated optical pump through the photothermal effect. The ensuing vibrational response of the array is multiplexed onto a single probe beam in the form of a high frequency phase modulation. The phase modulation is optically down converted to a low frequency intensity modulation using an adaptive full-field interferometer, and subsequently detected using a CCD array. Rapid and single step mechanical characterization of ~44 nominally identical high-frequency resonators is demonstrated. The technique may enable sensitivity improvements over single NEMS resonators by averaging signals coming from a multitude of devices in the array. In addition, the diffraction limited spatial resolution may allow for position-dependent read-out of NEMS sensor chips for sensing multiple analytes or spatially inhomogeneous forces.

KEYWORDS: NEMS arrays, optomechanics, nanomechanics, optical transducer, interferometry

Resonant nanoelectromechanical systems (NEMS) have been employed in impressive fundamental experiments in order to measure quantum zero-point oscillations,¹ physical forces^{2,3} and electron spin flips.⁴ Potential applications of NEMS extend from single biomolecule sensing^{5–7} to electromechanical signal processing⁸ to computation.^{9,10} Most of these experiments and application efforts have remained on single devices — barring a few notable exceptions.^{11–13} Yet, the real impact of NEMS is expected^{14,15} to come from arrays of many resonators working in concert over the scale of a chip. This is because a single NEMS resonator has very small linear dimensions; it possesses only a minute active sensing area, generates a motional signal typically buried in noise and can handle a tiny amount of power. To counteract these adversities while retaining sensitivity, one must employ an array of resonators. In sensing applications, for instance, the active area would increase linearly with the number of resonators in the array, more power could be dissipated over an array, and not only would there be more coherent signal available from an array (e.g., from synchronized oscillations of resonators) but the signal to noise ratio would grow as well. Thus, development of versatile nanotechnologies to operate NEMS arrays distributed over the scale of a chip is essential for further progress in this field.

Operation of arrays of NEMS resonators still constitutes a significant challenge, even though optical^{16,17} and electronic^{18,19} transducers have successfully been applied to single NEMS resonators. In particular, read-out or detection of the tiny oscillations of NEMS is the main technical hurdle.²⁰ An efficient and desirable approach to operate NEMS arrays is to multiplex all excitation and response signals from individual resonators onto a single channel and decode the response at the detection end. Such multiplexed detection of NEMS resonators has recently been demonstrated over electrical and optical channels.^{11,12} In

both, however, obtaining spatial resolution, that is, determining which particular resonators in the array are moving at a given frequency, has not been possible. Lack of spatial resolution imposes further limitations on the detection; if the resonances of the individual NEMS resonators are not well-separated in frequency or are degenerate, detection of multiple resonances is not straightforward. This is not detrimental in vacuum, because even identically fabricated resonators almost always have well-separated resonances due to their high quality (*Q*) factors. But the situation changes dramatically in fluids, where the *Q*s are significantly lower.^{21,22} Furthermore, aiming toward applications where synchronized oscillations of many resonators on a chip are desired,²³ spatial resolution is an indispensable element in array read-out techniques. Here we describe an all optical technique for interfacing with NEMS arrays. Our technique mitigates some of the above-described problems in operation of NEMS arrays. First, we demonstrate multiplexed actuation and detection of a NEMS array. Second and perhaps more importantly, we maintain excellent spatial resolution.

Our optical transduction technique for the detection of NEMS array motion is based on adaptive holographic interferometry,^{24,25} which makes use of a photorefractive crystal²⁶ as the optical recording media. The photorefractive crystal can be configured as an optical mixer and low-pass filter,^{27,28} or an optical lock-in amplifier, allowing for high-frequency phase modulation induced on an optical beam to be down-converted to a low frequency intensity modulation that can be detected with a conventional charge-coupled device (CCD) array. Furthermore, operating in full-field mode,^{29–31} the vibration of each

Received: October 30, 2010

Revised: December 29, 2010

Published: February 02, 2011

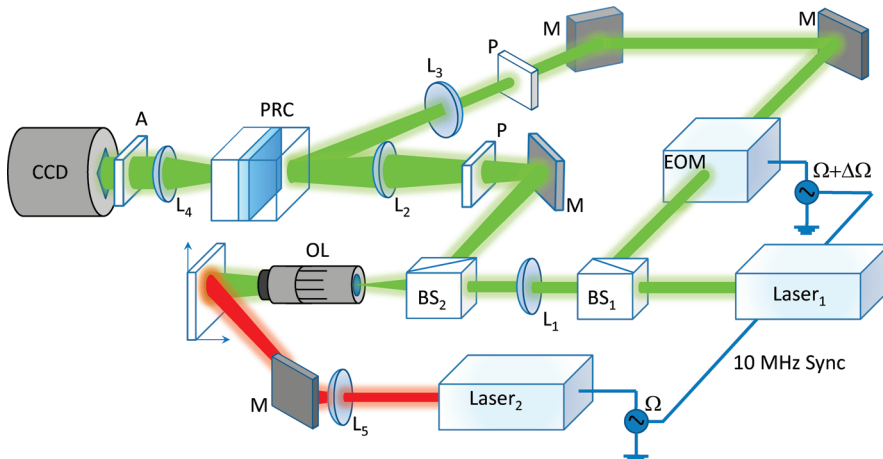


Figure 1. Schematic of the experimental set up. The path of the detection laser (Laser₁) is shown in green while that of the excitation laser (Laser₂) is shown in red. Electrical connections are shown in blue. The following component labels are used: L₁–L₅, lenses; BS₁ and BS₂, beamsplitters; P, polarizer; OL, 50× microscope objective; M, mirror; EOM, electro-optic modulator; A, polarization analyzer.

point on the sample is mapped to an intensity modulation at a corresponding pixel of the CCD with the amplitude of the modulation linearly proportional to the displacement. This offers the possibility of simultaneous interrogation of large scale arrays of devices. Finally, the adaptive nature of a photorefractive crystal refers to the fact that it actively responds to changes in incident optical fields, offering isolation from ambient vibration within the response time of the crystal and eliminating the need for active stabilization of the interferometer. Full-field adaptive holographic interferometry using optical lock-in detection has been used in the past for such applications as imaging modes of vibration on macroscopic disks and MEMS resonators, and imaging traveling Lamb waves in a plate.^{30,31}

A schematic of our experimental setup is shown in Figure 1. A diode laser source with an integrated electro-absorption modulator (EAM) and operating at a wavelength of 1550 nm is used to excite vibration of the NEMS devices through the photo-thermal effect.³² The output of the laser is amplified to 3.5 W using a fiber-coupled optical amplifier and is subsequently directed through a lens to the sample surface. The beam impinges on the surface at an angle producing an elliptical spot with a Gaussian profile with major and minor axes of 180 and 160 μm , respectively. A signal generator is used to drive the EAM, producing a sinusoidal intensity modulation of the light at a given drive frequency Ω . The interferometer uses a 200 mW frequency doubled Nd:YAG laser operating at a wavelength of 532 nm. The output of the laser is sent to a variable beam splitter where it is divided into a signal beam and a reference beam. The signal beam is sent through a spatial filter to a lens ($f = 350$ mm), where it is focused on the back surface of a 50× long working distance objective with a numerical aperture of 0.42. This produces a broad illumination spot at the focal plane of the objective with a diameter of approximately 400 μm . Light reflected from the sample travels back through the objective and is directed through the photorefractive crystal and a polarizer to the CCD camera. Lenses (L₂ and L₄) are used to create an image of the sample surface at the plane of the CCD. The reference beam is sent through a broadband electro-optic phase modulator, which is driven at a frequency $\Omega + \Delta\Omega$ using a signal generator and a power amplifier. The beam is then directed to the

photorefractive crystal where it interferes with the signal beam, and beam coupling (two-wave mixing) takes place. The photorefractive crystal is bismuth silicon oxide (BSO) cut along the [001] and [110] directions with linear dimensions of 10 mm × 10 mm perpendicular to the optical axes and a thickness of 2.25 mm. The response time τ of the crystal under our experimental conditions is approximately 100 ms.

Here we give an overview of the operation of the interferometer and note that further details are available in the literature.²⁹ The out-of-plane motion at all points (x, y) on the sample induced by the excitation laser at frequency Ω is given by $z(x, y, \Omega) \cos 2\pi\Omega t$. This motion results in a phase modulation of the signal beam. The reference beam is also phase modulated at a frequency that is offset by a small amount $\Delta\Omega$ from the signal beam frequency, where $\Delta\Omega < 1/\tau$. Interference between the signal and reference beams at the photorefractive crystal produces a multitude of intensity gratings: (i) a static grating resulting from unshifted components of the signal and reference beams; (ii) a slowly moving grating resulting from interference between the frequency shifted component of the signal beam (sideband at Ω) and the reference beam frequency shifted by $\Omega + \Delta\Omega$; and (iii) a number of fast moving gratings that are beyond the response time of the crystal and hence suppressed. The static and slow moving intensity gratings are converted to refractive index gratings through the photorefractive effect. For small displacements, the strength of the slow moving grating is linearly proportional to the amplitude of the surface displacement. We read out the strength of this grating at each point in the photorefractive crystal through self-diffraction of the reference beam. The intensity of the diffracted reference beam is modulated at $\Delta\Omega$ as the slow moving grating is shifted in phase with respect to the dynamic grating, and this intensity modulation is detected using the CCD camera. We note that in this configuration anisotropic self-diffraction is employed such that the diffracted reference beam is rotated in polarization by 90° with respect to the transmitted signal beam and can thus be isolated using an analyzer;³³ this results in a significant reduction in the background light intensity at the camera. The net outcome is that the displacement at each point of the sample is imprinted at a particular point in the photorefractive crystal in the form of a phase grating and read out into a corresponding pixel of the CCD camera as an intensity modulation at $\Delta\Omega$.

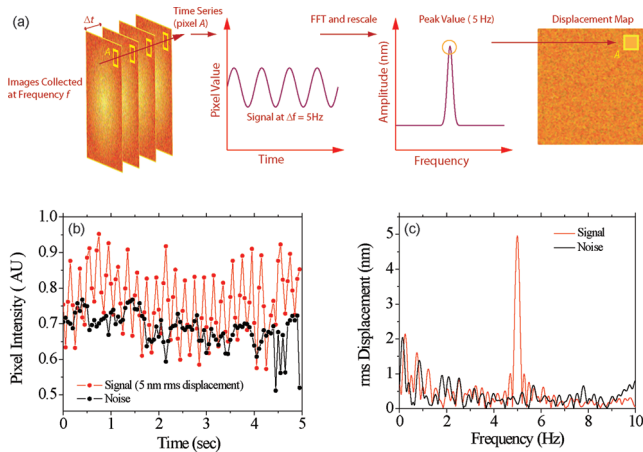


Figure 2. (a) Illustration of the processing steps used to create a displacement map. Multiple images are acquired at a sample rate of $1/\Delta t$ and the resulting time series is converted to the frequency domain using a FFT. The FFT (magnitude) peak is linearly proportional to the displacement. (b) Time traces of a typical pixel with rms sample displacements of 5 and 0 nm. (c) FFT of time traces in (b).

We now describe the technique used to form displacement maps of the sample surface. For the measurements reported here, the EOM is driven at $\Omega + 5$ Hz, where Ω is the signal frequency. It has been shown²⁹ that the intensity fluctuation at the CCD array for a small sample displacement is proportional to $J_0(\phi_r) J_1(\phi_r)$, where J_0 and J_1 are Bessel functions of the first kind and ϕ_r is the phase shift of the reference beam imparted by the EOM. The EOM is set to impart a phase modulation of 1.08 radians to maximize the value of this product. The procedure used to create displacement maps of the sample surface is illustrated in Figure 2a. N images were captured with a delay time between image acquisition of $\Delta t = \eta + \eta/4$, where $\eta = 200$ ms is the period of the signal at 5 Hz. The time domain trace from each pixel was processed using a fast Fourier transform (FFT), and the magnitude of the FFT at 5 Hz was converted to normal displacement of the sample surface. The system was calibrated by placing a mirror mounted on a piezo-actuator in the sample plane and subjecting the mirror to a known displacement. Prior to the experiment, the mirror motion as a function of drive voltage had been determined using a path stabilized Michelson interferometer. The calibration was performed with $N = 100$ images (25 cycles), a mean intensity of $I_p = 9.4$ pW incident on each pixel, and a displacement amplitude of 5 nm. A time trace from a representative pixel is shown in the red curve in Figure 2b, where the intensity fluctuation at 5 Hz is evident. The magnitude of the FFT of the signal from this same pixel is shown in Figure 2c, from which the value at 5 Hz was selected. For the calibration, the mean magnitude measured over the pixel array, was assigned a value of 5 nm. The displacements reported in the experimental results were based on this calibration, and appropriately scaled based on the selected N and measured I_p .

The system noise was characterized through measurement of the mean effective displacement in the absence of sample motion under the same experimental conditions described above for the calibration. The mean noise amplitude, converted to effective displacement using the calibration factor, was found to be equal to 103 pm under these experimental conditions. Given a detection bandwidth of ~ 0.2 Hz, this gives a minimum detectable displacement, at which the signal-to-noise ratio is equal to unity,

of 230 pm $\text{Hz}^{-1/2}$. Each pixel size is ~ 219 nm, and thus the power incident on each pixel is quite low when illuminating the full field with the given laser source, leading to the moderate displacement sensitivity. One can benchmark the system against an ideal classical homodyne interferometer operating in the shot noise limit, which has a displacement sensitivity under these operating conditions of approximately 10.8 pm $\text{Hz}^{-1/2}$. The discrepancy between the two values stems from additional noise sources in our experiment, including the ambient vibrations not being completely compensated for by the photorefractive crystal, and the intensity and the phase noise in the laser dominating over the shot noise in the system. We note that further reduction in the minimum detectable displacement can be achieved through decreasing the measurement bandwidth (through increasing N) or by increasing the mean light intensity incident on the CCD.

We now turn to a demonstration of multiplexed detection of photothermally driven motion on a NEMS array using adaptive holographic interferometry. Figure 3a shows the SEM micrographs of the array device used in these experiments. The array consists of 60 doubly clamped beams arranged in four rows with 15 beams each. The array is fabricated using standard top-down techniques. All the beams in the array have identical nominal dimensions of $10\ \mu\text{m}$ in length, $1\ \mu\text{m}$ in width, and a $200\ \text{nm}$ thickness, comprised of $150\ \text{nm}$ of structural Si coated with a $50\ \text{nm}$ Cr film. All beams are simultaneously excited through the photothermal effect using the distributed excitation laser intensity modulated at a single frequency Ω . A set of 1000 images (250 cycles of vibration at 5 Hz) are collected and processed to produce a displacement map. Figure 3b,c shows the results of this process at excitation frequencies of $\Omega \approx 21.5$ and $22.0\ \text{MHz}$, respectively. These maps are formed by plotting the rms displacement at each point (x,y) on the surface at Ω using the RGB color code shown. The plots show a $98\ \mu\text{m} \times 85\ \mu\text{m}$ region in the center of the array, covering 44 beams. At a given frequency, the recorded displacements are very nonuniform throughout the sample: several beams show high amplitude oscillations, while the rest of the array is hardly moving. This is because the resonance frequencies of the beams are spread over a substantial frequency band even though the nominal dimensions are identical. Figure 3d shows a zoomed-in view ($6\ \mu\text{m} \times 16\ \mu\text{m}$) of one of the beams vibrating in the fundamental mode close to the resonance frequency. From this image, one can select a given region of interest and track the surface displacement amplitude as a function of frequency. Such a result is illustrated in Figure 3e, where the excitation frequency was scanned from 20 to $23.8\ \text{MHz}$ in steps of $0.1\ \text{MHz}$ and the mean displacement over 3×3 pixels in the center of the beam is plotted as a function of frequency. The resonance peak lies at $22.0\ \text{MHz}$ and $Q \approx 48$ is consistent with atmospheric damping.²¹

The full extent of the data collected using this powerful technique is harder to visualize. At each frequency Ω and for each surface point (x,y) , a root-mean-square (rms) displacement is recorded, providing a $451 \times 391 \times 43$ matrix of displacements $z(x,y,\Omega)$. To better show the “depth” of our data, we have created the “cross sections” shown in Figure 4a. The base of Figure 4a shows the photorefractive image of the array at $\Omega = 20\ \text{MHz}$, which is sufficiently far from any resonances. The two slices along the z -axis provide the frequency-progression of the rms displacements for the midpoints of the beams in rows one and four. In principle, each of the bright lines along Ω represents a plot similar to that shown in Figure 3e, but with the Lorenzian line shape plotted in the given color scale and the brightest point

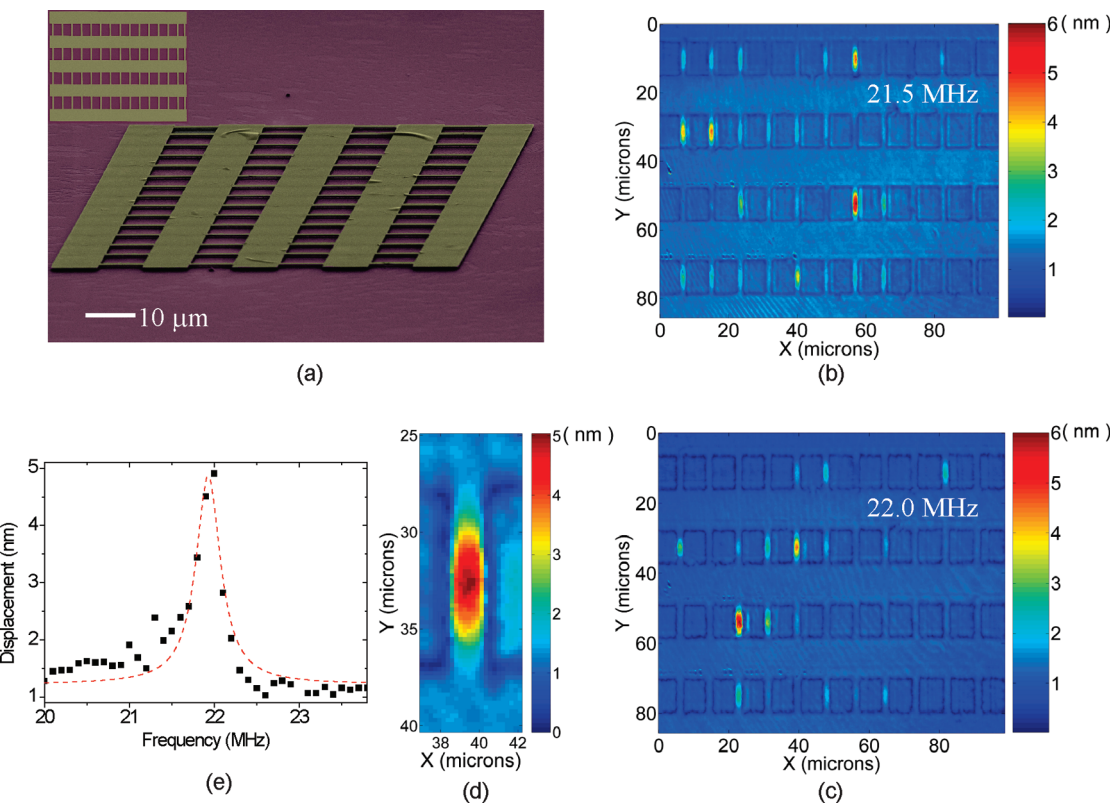


Figure 3. (a) SEM micrographs showing top and oblique views of the 60 element NEMS array. (b,c) The displacement images of the array at excitation frequencies of 21.5 and 22.0 MHz, respectively. (d) A zoomed in displacement map of a single beam operating at its fundamental frequency. (e) The spectral response of the beam shown in (d) found by averaging the displacement of the central 3×3 pixels and sweeping the frequency.

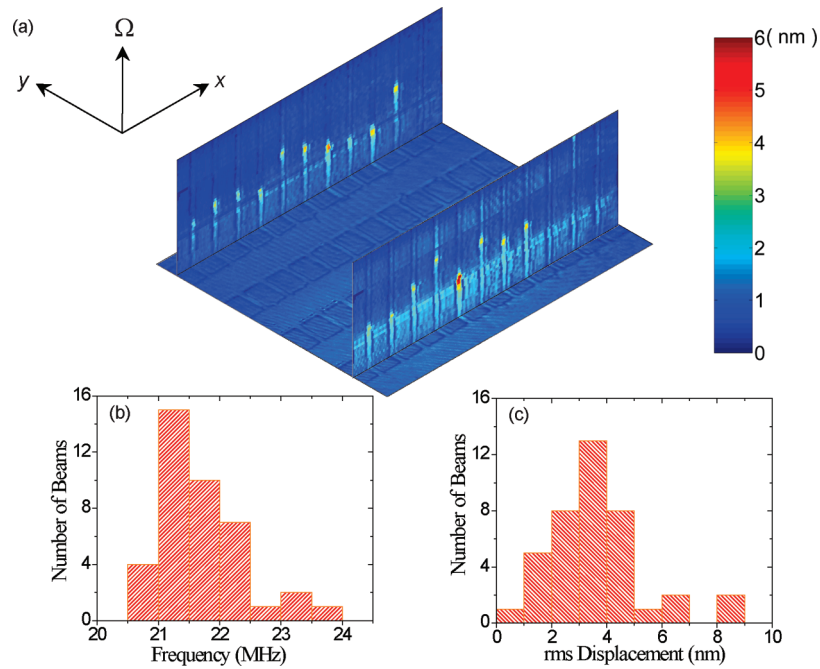


Figure 4. (a) A spatiotemporal map of the array with the base displacement image at 20.0 MHz and slices across rows of beams showing the response as a function of frequency over a 20.0–24.2 MHz frequency range. (b,c) Histograms of the array resonance frequency and peak displacement amplitude, respectively.

corresponding to the resonance frequency. The data presented in Figure 4a thus correspond to two reduced $\sim 451 \times 43$

submatrices of the full three-dimensional matrix. This means of representing the data allows for a basic visual inspection of the

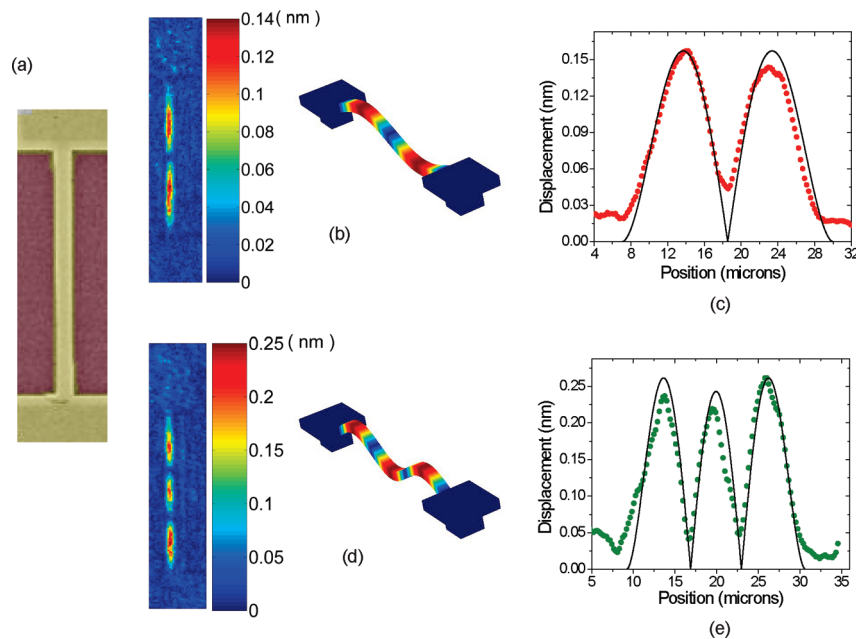


Figure 5. (a) SEM micrograph showing a top view of a $20\ \mu\text{m}$ long and $1\ \mu\text{m}$ wide resonator. (b) The experimental displacement map and a FEM simulation of the mode shape for the beam vibrating at its first harmonic mode at a frequency of $14.5\ \text{MHz}$. (c) The measured mode shape for the first harmonic mode. (d) The displacement map and a FEM simulation of the mode shape at $28\ \text{MHz}$, showing the beam vibrating at its second harmonic mode. (e) The measured mode shape for the second harmonic mode.

collective behavior of the array elements. Various metrics of array performance can be easily extracted from the full displacement matrix. For example, in Figure 4b we show a histogram of the resonance frequencies, and in Figure 4c we show a histogram of the peak displacement amplitudes measured in each beam. The histogram includes results from 40 beams; the motion of the remaining 4 beams was found to be below the noise level of the system leading us to believe that they may not be operational.

Optical excitation and full-field optical detection allows for massively multiplexed detection of device motion while at the same time offering excellent spatial resolution. In addition to exciting and detecting the fundamental modes of nanomechanical structures, we have also demonstrated the ability to interface with higher modes. Figure 5a shows a $20\ \mu\text{m}$ long and $1\ \mu\text{m}$ wide beam used for these experiments. The thickness of the beam was $320\ \text{nm}$, which is comprised of $280\ \text{nm}$ of structural silicon coated with $40\ \text{nm}$ of Cr. The beam was excited using an optical power density of $9.4\ \text{W/mm}^2$ and $N = 4000$ (1000 cycles at $5\ \text{Hz}$) images were collected and processed. Figure 5b shows the displacement of the beam operating at the peak frequency of its first harmonic resonance at $14.5\ \text{MHz}$ with a schematic of the mode shape included for comparison. The mode shape along the beam, found by spatially averaging the displacement response over a moving 3×5 pixel (width by length, where 1 pixel $\sim 219\ \text{nm}$) window is shown in Figure 5c. The peak displacement observed for the second mode is $150\ \text{pm}$. Figure 5d,e gives analogous results for the second harmonic at a frequency of $28\ \text{MHz}$ showing the displacement map and mode shape, respectively. The ability to excite and detect multiple modes using this approach may prove useful in mass sensing applications, where the use of higher modes can lead to increases in sensitivity and functionality of NEMS devices.³⁴

The technique presented here has proven applicable over a large spatial dynamic range. The above data unequivocally demonstrate displacement detection over an area having the size

of a typical device chip, $\sim 120\ \mu\text{m} \times 120\ \mu\text{m}$. At the opposite end of the spatial dynamic range is the measurement of displacement signals coming from sources in close proximity. As with all far-field optical techniques, the ability to resolve the displacement of two closely spaced resonators is ultimately limited by diffraction to $\sim 0.61\lambda/\text{NA}$, where NA is the numerical aperture of the objective lens. In our experiments, this requires a separation of about $770\ \text{nm}$ between devices. However, detection of the displacement of single resonators that have smaller characteristic length scales is possible, so long as sufficient scattered light is collected from the device to overcome the noise sources in the system for a given integration time. With the modest device linear dimensions of Figure 3a and a $1\ \mu\text{m}$ separation between beams, we estimate that our experimental system shown here could be used to interface with ~ 1000 beams, simultaneously. We also note that the requirements on optical alignment, which can be quite severe when using tightly focused laser sources to detect the motion of a single point on a device, are relaxed in the full field measurement. In the latter case, the region of interest on the chip need simply be placed at any point within the field of view of the microscope.

Finally, we discuss how arrayed NEMS resonators could improve detection limits available from single NEMS resonators. Let us first consider a generic mass sensing experiment involving a single NEMS resonator: here, one carefully measures the resonance frequency of the device before and after perturbing it by adding a small mass. A prior calibration is then used to quantify the perturbing mass. In frequency-shift-based sensing, a signal-to-noise ratio of 1 corresponds to a measurement of a frequency shift equal to the (intrinsic or extrinsic) frequency fluctuations of the resonator δf . Now, we consider the same measurement using an array with M resonators, assuming that our set up and measurement noise could be optimized in a next-generation experiment to provide a frequency resolution comparable to state-of-the-art.⁵ Now, if each resonator receives the

same added mass, for instance, by a spatially uniform analyte coverage, one obtains $\delta f/\sqrt{M}$ and hence a mass resolution reduced by a factor of $1/\sqrt{M}$. The real advantage of an array, however, becomes manifest in cases where the analyte molecules are very rare. If the active area (capture area) of a single resonator is S , the array improves this to MS , reducing greatly the time to obtain a signal. Similar considerations apply to force sensing as well. Here, one measures the amplitude or the frequency of the resonator before and after turning on a force field, depending on whether one is measuring a resonantly coupled force or a dc force field. Again, in the simple case of a spatially uniform force one obtains a $1/\sqrt{M}$ reduction in the minimum detectable force. If the force is spatially nonuniform, then an array can allow for the detection of the force-map rapidly, perhaps without the need for scanning the probe (the NEMS resonators).

AUTHOR INFORMATION

Corresponding Author

*E-mail:(K.L.E)ekinci@bu.edu;(T.W.M.)todd.murray@colorado.edu.

ACKNOWLEDGMENT

A.S. acknowledges a graduate fellowship from the Boston University Photonics Center. K.L.E. acknowledges support from the U.S. National Science Foundation (NSF) through Grant ECCS-0643178. T.W.M and K.L.E. also acknowledge support through NSF grant ECCS-0609010.

REFERENCES

- (1) O'Connell, A. D.; et al. Quantum ground state and single-phonon control of a mechanical resonator. *Nature* **2010**, *464*, 697–703.
- (2) Li, M.; et al. Harnessing optical forces in integrated photonic circuits. *Nature* **2008**, *456*, 480–484.
- (3) (a) Li, M.; Pernice, W. H. P.; Tang, H. X. Tunable bipolar optical interactions between guided lightwaves. *Nat. Photonics* **2009**, *3*, 464. (b) Roels, J.; et al. Tunable optical forces between nanophotonic waveguides. *Nat. Nanotechnol.* **2009**, *4*, 510–513.
- (4) Rugar, D.; Budakian, R.; Mamin, H. J.; Chui, B. W. Single spin detection by magnetic resonance force microscopy. *Nature* **2004**, *430*, 329–332.
- (5) Naik, A. K.; Hanay, M. S.; Hiebert, W. K.; Feng, X. L.; Roukes, M. L. Towards single-molecule nanomechanical mass spectrometry. *Nat. Nanotechnol.* **2009**, *4*, 445–450.
- (6) Ilic, B.; et al. Attogram detection using nanoelectromechanical oscillators. *J. Appl. Phys.* **2004**, *95*, 3694–3703.
- (7) Jensen, K.; Kim, K.; Zettl, A. An atomic-resolution nanomechanical mass sensor. *Nat. Nanotechnol.* **2008**, *3*, 533–537.
- (8) Mahboob, I.; Yamaguchi, H. Bit storage and bit flip operations in an electromechanical oscillator. *Nat. Nanotechnol.* **2008**, *3*, 275–279.
- (9) Roukes, M. L. Mechanical Computation, Redux? *IEEE Int. Electron Devices Meet., Tech. Dig.* **2004**, 539–542.
- (10) Blick, R. H.; Qin, H.; Kim, H.-S.; Marsland, R. A nanomechanical computer—exploring new avenues of computing. *New J. Phys.* **2007**, *9*, 241.
- (11) Truitt, P. A.; et al. Efficient and Sensitive Capacitive Read-out of Nanomechanical Resonator Arrays. *Nano Lett.* **2007**, *7*, 120.
- (12) Li, M.; Pernice, W. H. P.; Tang, H. X. Broadband all-photonic transduction of nanocantilevers. *Nat. Nanotechnol.* **2009**, *4*, 377–382.
- (13) Zalalutdinov, M. K.; et al. Two-dimensional array of coupled nanomechanical resonators. *Appl. Phys. Lett.* **2006**, *88*, No. 143504.
- (14) Lutwyche, M. I.; Despont, M.; Drechsler, U.; Durig, U.; Haberle, W.; Rothuizen, H.; Stutz, R.; Widmer, R.; Binnig, G. K.; Vettiger, P. Highly parallel data storage system based on scanning probe arrays. *Appl. Phys. Lett.* **2000**, *77*, 3299.
- (15) Salaita, K.; Wang, Y.; Fragala, J.; Vega, R. A.; Liu, C.; Mirkin, C. A. Massively Parallel Dip-Pen Nanolithography with 55 000-Pen Two-Dimensional Array. *Angew. Chem., Int. Ed.* **2006**, *45*, 7220–7223.
- (16) Liu, N.; Giesen, F.; Belov, M.; Losby, J.; Moroz, J.; Fraser, A. E.; McKinnon, G.; Clement, T. J.; Sauer, V.; Hiebert, W. K.; Freeman, M. R. *Nat. Nanotechnol.* **2008**, *3*, 715–719.
- (17) Thourhout, D. V.; Roels, J. Optomechanical device actuation through the optical gradient force. *Nat. Photonics* **2010**, *4*, 211–217.
- (18) Masmanidis, S. C.; Karabalin, R. B.; De Vlaminck, I.; Borghs, G.; Freeman, M. R.; Roukes, M. Multifunctional nanomechanical systems via tunably coupled piezoelectric actuation. *Science* **2007**, *317*, 780.
- (19) Unterreithmeier, Q. P.; Weig, E. M.; Kotthaus, J. P. Universal transduction scheme for nanomechanical systems based on dielectric forces. *Nature* **2009**, *458*, 1001–1004.
- (20) Ekinci, K. L. Electromechanical Transducers at the Nanoscale: Actuation and Sensing of Motion in Nanoelectromechanical Systems (NEMS). *Small* **2005**, *1*, 786.
- (21) Karabacak, D.; Yakhot, V.; Ekinci, K. L. High-Frequency Nanofluidics: An Experimental Study Using Nanomechanical Resonators. *Phys. Rev. Lett.* **2007**, *98*, No. 254505.
- (22) Venstra, W. J.; Westra, H. J. R.; Babaei Gavan, K.; van der Zant, H. S. J. Magnetomotive drive and detection of clamped-clamped mechanical resonators in water. *Appl. Phys. Lett.* **2009**, *95*, No. 263103.
- (23) Cross, M. C.; Zumdieck, A.; Lifshitz, R.; Rogers, J. L. Synchronization by nonlinear frequency pulling. *Phys. Rev. Lett.* **2004**, *93*, No. 224101.
- (24) Ing, R. K.; Monchalin, J. P. Broadband detection of ultrasound by two wave mixing in a photorefractive crystal. *Appl. Phys. Lett.* **1991**, *59*, 3233.
- (25) Delaye, P.; Blouin, A.; Drolet, D.; de Montmorillon, L.-A.; Roosen, G.; Monchalin, J. P. Detection of ultrasonic motion of a scattering surface by photorefractive InP:Fe under an applied dc field. *J. Opt. Soc. Am. B* **1997**, *14*, 1723–1734.
- (26) Solymar, L.; Webb, D. J.; Grunnet-Jepsen, A. *The Physics and Applications of Photorefractive Materials*; Clarendon Press: Oxford, 1996.
- (27) Khouri, J.; Ryan, V.; Woods, C.; Cronin-Golomb, M. Photorefractive optical lock-in detector. *Opt. Lett.* **1991**, *16* (8), 1442.
- (28) Khouri, J.; Kane, J. S.; Kierstead, J.; Woods, C.; Hemmer, P. Real time holographic baseband frequency demodulator. *Appl. Opt.* **1994**, *33* (14), 2909.
- (29) Hale, T. C.; Telschow, K. L.; Deaton, V. A. Photorefractive optical lock-in vibration spectral measurement. *Appl. Opt.* **1997**, *36* (31), 8248.
- (30) Telschow, K. L.; Deaton, V. A.; Cottle, D. L.; Larson, J. D., III Full-field imaging of Gigahertz Film Bulk Acoustic Resonator Motion. *IEEE Trans. Ultrason., Ferroelectr., Freq. Contr.* **2003**, *50* (10), 1279.
- (31) Telschow, K. L.; Deaton, V. A.; Schley, R. S.; Watson, S. M. Direct Imaging of Lamb waves in plates using photorefractive dynamic holography. *J. Acoust. Soc. Am.* **1999**, *106* (5), 2578.
- (32) Sampathkumar, A.; Murray, T. W.; Ekinci, K. L. Photothermal operation of high frequency nanoelectromechanical systems. *Appl. Phys. Lett.* **2005**, *88*, No. 223104.
- (33) Troth, R. C.; Dainty, J. C. Holographic interferometry using anisotropic self-diffraction in $\text{Bi}_{12}\text{SiO}_{20}$. *Opt. Lett.* **1991**, *16* (1), 53.
- (34) Dohn, S.; Sandberg, R.; Svendsen, W.; Boisen, A. Enhanced functionality of cantilever based mass sensors using higher modes. *Appl. Phys. Lett.* **2005**, *86*, No. 233501.